Flare in Interference-Based Hyperspectral Cameras

Eden Sassoon, Yoav Y. Schechner
Viterbi Faculty of Electrical Engineering
Technion - Israel Institute of Technology
Haifa, Israel

eden.sas8@gmail.com, yoav@ee.technion.ac.il

Tali Treibitz
Charney School of Marine Sciences
University of Haifa
Haifa, Israel

ttreibitz@univ.haifa.ac.il

Abstract

Stray light (flare) is formed inside cameras by internal reflections between optical elements. We point out a flare effect of significant magnitude and implication to snapshot hyperspectral imagers. Recent technologies enable placing interference-based filters on individual pixels in imaging sensors. These filters have narrow transmission bands around custom wavelengths and high transmission efficiency. Cameras using arrays of such filters are compact, robust and fast. However, as opposed to traditional broad-band filters, which often absorb unwanted light, narrow band-pass interference filters reflect non-transmitted light. This is a source of very significant flare which biases hyperspectral measurements. The bias in any pixel depends on spectral content in other pixels. We present a theoretical image formation model for this effect, and quantify it through simulations and experiments. In addition, we test deflaring of signals affected by such flare.

1. Introduction

Hyperspectral imagers are increasingly used in computer vision [3, 5, 6, 14, 20, 25, 27, 29], as in other imaging domains, e.g. remote sensing [15], ecology [21, 30] and biomedical imaging. Various architectures of hyperspectral cameras have different tradesoffs of spatial/spectral/temporal resolutions and light gathering efficiency (i.e., signal to noise ratio). For example, RGB cameras have high spatiotemporal resolution but poor spectral resolution (only three wide bands). Line-scan hyperspectral cameras have high spatio-spectral resolution but scanning slows acquisition, hence limiting temporal resolution. Recent technological developments enable snapshot hyperspectral cameras (SHYCs) which are fast, compact, robust and especially suitable for autonomous vehicles. They are based on a set of pixel-sized narrow-band interference filters that are mounted directly over high-resolution sensors, behind a lens [1, 11, 17, 23, 28]. SHYCs sacrifice some
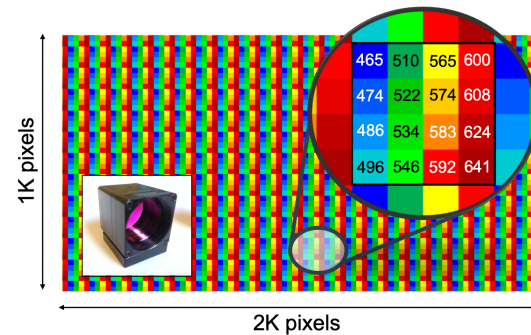

Figure 1. An example of 16 narrow-band interference filters [26] mounted onto a detector array in the Imec SNm4x4 VIS sensor. Each batch of 16 filters is mounted in a mosaic of 4×4 pixels, which generalizes the 2×2 Bayer pattern of RGB cameras. Such a sensor trades off spatial resolution for increased spectral resolution. However, interference filters are highly reflective. [Insert] The XIMEA MQ022HG-IM-SM4X4-VIS C-mount camera that features this sensor, used in our experiments.

spatial resolution for spectral resolution, as shown in Fig. 1.

In this paper we show that such sensors bear a significant degradation (see Fig. 2): stray light (flare), which is much stronger than lens-flare encountered in traditional technologies. Hyperspectral cameras generally seek to resolve well defined, narrow spectral bands. However, the transmitted signal energy decreases as a pass-band narrows. Hence, there is an important need for efficiency of light transfer, minimizing energy loss in the spectral band that passes to the detector. Meeting these two needs can be engineered using established theory and tools, based on *interference*. Interference filters have very efficient optical transfer, and can yield very narrow bands. These filters are sometimes termed Fabry-Pérot (FP) etalons [7]. However, we point out a caveat in the context of imaging: FP filters in use have very high reflectivity. This leads to very strong flare.

Flare also exists in everyday RGB cameras and has been studied both in the computer vision and graphics communi-
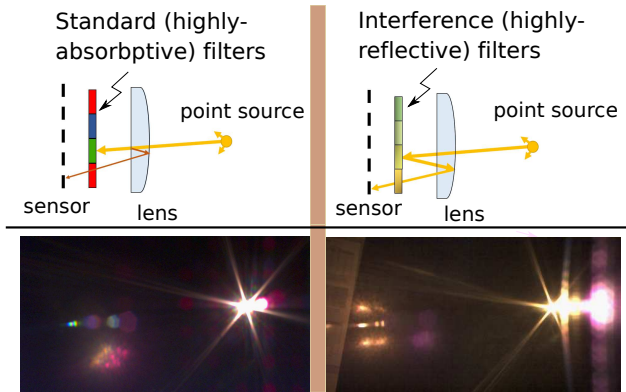
Figure 2. [Left] In standard RGB cameras, filters are absorptive. Lens-flare is a weak second-order effect, of significance only if the source is very bright. [Right] Interference filters used in a snapshot hyperspectral camera (SHYC) are highly reflective, creating strong flare from ordinary scene points.

ties. However, regular cameras use absorbing filters. Then, flare stems from internal lens reflections, requiring at least two bounces in the lens system to reach the camera (See Fig. 2). It is thus termed *lens-flare* and is significant only when originating from strong light sources, e.g., sunlight. Contrary to that, as we show, interference filters reflect light so strongly, that even a single-bounce from a lens results in strong flare. We analyze the image formation and demonstrate through simulations and experiments that the magnitude of flare induced by interference filters (FIIF) is several percents of the desired signal.

Lens flare - independent of FIIF - has been modelled [8] and analyzed in computer vision, optics and computer graphics literature. Ref. [22] proposes a method for assessing and subtracting lens-flare using an external movable occluding mask. Lens flare typically lies on straight lines [12], passing through the image-plane projection of the optical axis and the light source (sun). Using this insight and a few images taken while the camera moves, lens-flare can be partly estimated, compensated for and even exploited for assessing these geometric entities [12]. This is useful for computer vision. These approaches can be used also to partly counter FIIF. Lens-flare removal has been considered using additional methods, including light-field cameras [18], Bayesian [24] or exemplar-based image-inpainting [4].

2. Theoretical Background

In this section we describe prior optical models that have thus far been considered separately: the optical transfer of interference-based spectral filters, and lens flare in cameras. In Sec. 3, flare is shown to be much stronger when these optical filters are used inside a camera.
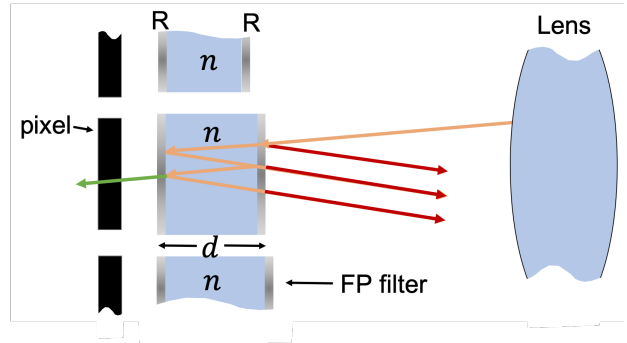

Figure 3. An FP etalon comprises a dielectric medium having index of refraction n and thickness d between reflective (partial mirror) surfaces having reflectance R. Various reflection orders interfere. Overall FP transmissivity and reflectivity can be designed for narrow pass-bands.

2.1. Fabry-Pérot Filters

A simple model for an FP etalon is as follows [9]. A layer of lossless dielectric material has refractive index n and thickness d. Light of wavelength λ passing through the layer at angle $\theta_{\rm c}$ relative to the normal accumulates phase

$$\delta = \frac{2\pi n}{\lambda} d \cos \theta_{\rm c} . \tag{1}$$

Suppose the layer is sandwiched between two mirrors. Each mirror has intensity reflectivity R, i.e. reflection is partial. Consequently, light which is inside the dielectric layer is partly trapped there, being reflected multiple times (up to infinity) back and forth between the mirrors. In each internal reflection round (*reflection order*) at the FP etalon, phase is further accumulated.

As each of the mirrors has partial reflectivity, it also has partial transmissivity. In lossless mirrors, all energy which is not reflected is transmitted, and vice versa. In each FP internal-reflection order, some light leaks out of the etalon, interfering with light of other reflection or transmission orders (Fig. 3). This interference either enhances or inhibits the overall transmissivity and reflectivity of the FP-etalon, given respectively by the expressions

$$T_{\rm FP}(\lambda) = \left[1 + \frac{4R}{(1-R)^2} \sin \left(\frac{2\pi n}{\lambda} d \cos \theta_{\rm c} \right) \right]^{-1} , \tag{2}$$

$$R_{\rm FP}(\lambda) = 1 - T_{\rm FP}(\lambda) . \tag{3}$$

Generally, an interference filter can be more complex. It can be made of multiple layers, each having a different refractive index, thickness, and have some loss. However, the general properties of interference filters used in SHYCs are similar to those expressed in Eqs. (2,3):

(A) Strong reflection of non-transmitted light. Efficient transmission in the pass-band of the filter.
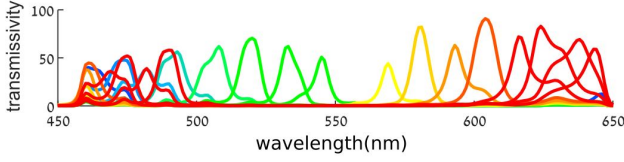
Figure 4. Calibrated transmissivity of the 16 narrow-band filters used in our commercial sensor (Fig. 1). This data corresponds to normal incidence. Data provided by the sensor manufacturer.

(B) The FP reflectivity and transmissivity strongly depend on the wavelength. As an example, Fig. 4 plots the transmissivity of the 16 narrow-band filters used in our commercial sensor (Fig. 1). This dependence can be engineered by controlling the thickness and material of each layer in each filter.

(C) The selectivity of a filter is defined by its *finesse*. Corresponding to the simple FP setup above, the finesse is defined by the unit-less expression

$$\mathcal{F} = \pi \left[2 \arcsin(1 - R)/(2^4 R) \right]^{-1} . \qquad (4)$$

The higher the finesse, the narrower the FP pass-band, and consequently the stronger is the overall reflectivity of all wavelengths outside this narrow pass-band.

(D) The FP optical transfer depends on the angle of incidence. Having incidence tilted relative to the layer normal biases the FP pass-band's central wavelength, and somewhat also biases the width of the pass-band.

2.2. Lens Flare

Lens flare[1] is a light transport phenomenon that occurs in lenses [19]. As light traverses refractive elements in an optical imaging system (lens elements), abrupt changes of refractive index (particularly air/glass) induce weak partial back-reflections at refractive surfaces. The back-reflected light then traverses the optical system again, creating secondary weak reflections at the refractive surfaces. These secondary reflections propagate towards the detector array (Fig. 5a). Part of the energy of the secondary reflections reaches the detector array: this is *lens flare*. Another component of the secondary reflection repeats the process above, creating higher-order reflections which further contribute to flare, though with diminishing energy. Odd-order reflections direct energy out of the camera system.

The number of lens-elements in a compound camera lens is M. The total number of secondary reflections [13] (involving two surfaces) is $N_{\text{sec}} = M(2M-1)$. Let the image irradiance due to a scene source be I_{source}. Denote the typical reflectivity of a refractive surface as $R_{\text{lens}} \ll 1$. A secondary reflection (involving two surfaces) thus yields image

---

[1]Lens flare is also referred to in the literature as lens glare, ghost reflections and stray light. These terms are interchangeable in this context.
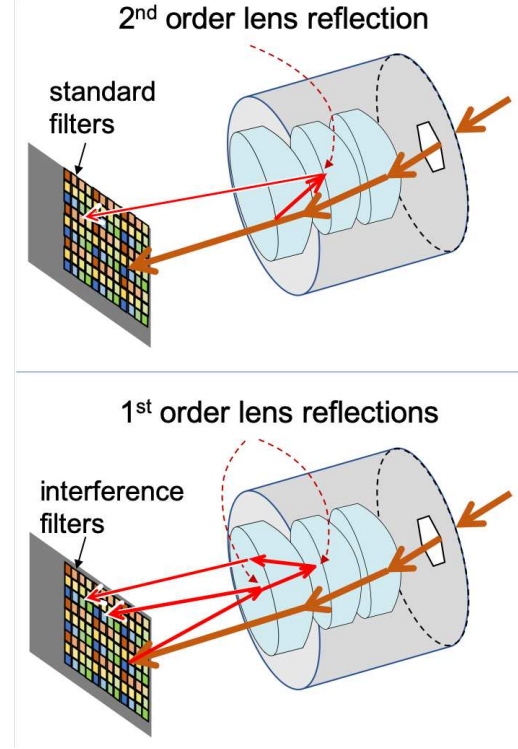

Figure 5. [Top] Lens flare forms by secondary internal reflections between lens surfaces. [Bottom] Light from the scene passes the lens barrel and strongly back-reflects at an interference filter inside the camera. The back-reflected light then makes a single reflection at a lens surface or iris. This can create a strong FIIF, which biases hyperspectral image measurements.

irradiance of an order $\mathcal{O}(I_{\text{source}} R_{\text{lens}}^2)$. A 4th-order reflection yields image irradiance of an order $\mathcal{O}(I_{\text{source}} R_{\text{lens}}^4)$. As $R_{\text{lens}} \ll 1$, all high order reflections are negligible, other than secondary reflections. The lens flare irradiance F_{lens} is thus of an order

$$\mathcal{O}(F_{\text{lens}}) \sim M(2M - 1)I_{\text{source}} R_{\text{lens}}^2 . \qquad (5)$$

Note that under typical illumination, flare *intensity* F_{lens} is incoherently added to the sensed image. Flare orders do not interfere as coherent wave amplitudes. This is contrary to reflection orders in a FP etalon, deliberated in Sec. 2.1. The reason for this distinction stems from the coherence length $\mathcal{L}$ of the incoming light. In natural lighting, $\mathcal{L} \gg dn$, where the FP thickness d is $\mathcal{O}(\text{micron})$, hence enabling interference through the FP etalon. On the other hand, the typical distance between lens element surfaces is $\mathcal{O}(\text{mm})$ which is longer than $\mathcal{L}$, thus inhibiting coherent amplitude interference between flare components.

For a simple glass/air interface, $R_{\text{lens}} \approx 4\%$. Anti-reflection lens coatings in essentially all modern imaging lenses reduce R_{lens} to $\approx 0.5\%$. Note, however, that anti-reflection coatings are based on the FP principle of

interference filtering, which makes them sensitive to the light wavelength. Hence from this point on, we denote lens reflectivity by $R_{\text{lens}}(\lambda)$. In these conditions, typically $\mathcal{O}(F_{\text{lens}}) \approx 10^{-4}I_{\text{source}}$. For typical scene objects, lens flare is thus negligible relative to flare-free scene radiance, I_{source}. For lens flare to be significant, it *must be created by a source which is orders of magnitude brighter* than darker regions [22] in the field-of-view (FOV). Specifically, the Sun is $\approx 10^5$ brighter [12] than sun-illuminated diffuse objects, hence the Sun is a common source of pronounced lens-flare.

In contrast to lens-flare F_{lens}, we show in the next sections that FIIF, denoted F_{FP}, is much more severe. It is significantly induced by ordinary scene points, everywhere. Moreover, F_{FP} is much brighter than F_{lens}, as it capitalizes also on first-order lens reflections.

3. Flare Due to Interference Filters

This section points out a new flare phenomenon, which is caused specifically by the presence of narrow bandpass interference filters inside a camera. Hence, this is an affect which is created inside SHYCs, in which camera pixels are directly overlayed with interference bandpass filters. This section further provides order-of magnitude analysis of the effect, theoretically indicating its severity. Afterwards, detailed analysis which accounts for the high orders of reflection, spatial pattern of a hyperspectral filter array and curvatures of elements in compound lenses is given by meticulous simulations in Sec. 4. Experiments demonstrate the effect in Sec. 5.

3.1. Single Reflection by a Lens

The analysis herein shows that FIIF is generally much stronger than lens flare, and is caused by all scene points, not only bright sources as the sun. An object having a source spectrum $I_{\text{source}}^{\mathbf{x}}(\lambda)$ is projected onto a filter-covered pixel $\mathbf{x}$ on the sensor plane. The filter's transmissivity and reflectivity are respectively $T_{\text{FP}}^{\mathbf{x}}(\lambda)$ and $R_{\text{FP}}^{\mathbf{x}}(\lambda)$, given in Eqs. (2,3). Define by $\mathcal{B}(\mathbf{x})$ the FP narrow spectral passband at $\mathbf{x}$. As mentioned above, SHYCs which rely on interference require narrow pass-bands (high finesse) and high transmissivity of the pass-band. Hence, $R_{\text{FP}}^{\mathbf{x}}(\lambda) \lesssim 1$, $\forall \lambda \notin \mathcal{B}(\mathbf{x})$.

For $\forall \lambda \notin \mathcal{B}(\mathbf{x})$, a major portion of the incident energy is thus back-reflected away from the detector array (Fig. 5b), with energy $\mathcal{O}[I_{\text{source}}^{\mathbf{x}}(\lambda)R_{\text{FP}}^{\mathbf{x}}(\lambda)] \approx I_{\text{source}}^{\mathbf{x}}(\lambda)$. The back-reflected light then partly reflects at any of the $2M$ refractive (lens) surfaces, as described in Sec. 2.2, shooting radiance towards the detector array, creating a flare component. Here, contrary to the model of Sec. 2.2, a *single reflection* off any single lens surface creates a significant flare irradiance (Fig. 5b). Due to the geometry of most refractive surfaces, this flare is dispersed over a region. FIIF projects generally beyond pixel $\mathbf{x}$, to pixel $\mathbf{y}$, for which the filter pass-band $\mathcal{B}(\mathbf{y}) \neq \mathcal{B}(\mathbf{x})$. Hence FP→lens reflections yield an FIIF component at $\mathbf{y}$, of order $\mathcal{O}[I_{\text{source}}^{\mathbf{x}}(\lambda)R_{\text{FP}}^{\mathbf{x}}(\lambda)R_{\text{lens}}(\lambda)T_{\text{FP}}^{\mathbf{y}}(\lambda)]$.

The FIIF at pixel $\mathbf{y}$ due to filter reflection at pixel $\mathbf{x}$ is denoted $F_{\text{FP}}^{\text{single}}(\mathbf{y}, \lambda | \mathbf{x})$. Accounting for single reflections from all $2M$ refractive surfaces, it is of order

$$\mathcal{O}[F_{\text{FP}}^{\text{single}}(\mathbf{y}, \lambda | \mathbf{x})] \sim \tag{6}$$
$$2MI_{\text{source}}^{\mathbf{x}}(\lambda)R_{\text{FP}}^{\mathbf{x}}(\lambda)R_{\text{lens}}(\lambda)T_{\text{FP}}^{\mathbf{y}}(\lambda).$$

For wavelengths that are in $\mathcal{B}(\mathbf{y})$ but not in $\mathcal{B}(\mathbf{x})$, $R_{\text{FP}}^{\mathbf{x}}(\lambda)T_{\text{FP}}^{\mathbf{y}}(\lambda) \lesssim 1$. Hence, Eq. (6) degenerates to

$$\mathcal{O}[F_{\text{FP}}^{\text{single}}(\mathbf{y}, \lambda | \mathbf{x})] \sim 2MI_{\text{source}}^{\mathbf{x}}(\lambda)R_{\text{lens}}(\lambda). \tag{7}$$

The result in Eqs. (6,7) is significant. It means that the spectral *sample at pixel $\mathbf{y}$ is biased due to contamination of spectral content from pixel $\mathbf{x}$*. Needless to say, pixel $\mathbf{y}$ is usually affected by FIIF not only due to reflection from pixel $\mathbf{x}$, but from many additional pixels. Hence, the bias is significant. FIIF does not necessitate a strong light source, contrary to lens-flare. For example, for $R_{\text{lens}} \approx 0.5\%$ (see Sec. 2.2) and $M = 7$ lens elements, the bias measures several percents. Since SHYCs are used mainly for demanding sensing applications, such a bias may have a significant effect on results of these applications, if not accounted for.

3.2. Double Reflection by Lenses

The interference filters mounted on the detector array create also significant secondary lens reflections. Consider the following sequence of reflections: FP→lens→FP→lens. The first reflection by a lens surface projects light towards the filter-covered detector array. There, pixel $\mathbf{z}$ reflects efficiently light back to the lens barrel. A secondary reflection by a lens surface projects light again towards the filter-covered detector array. Part of this light is captured by pixel $\mathbf{y}$. The analysis generalizes that of Sec. 3.1. Each such event creates a flare component of order $\mathcal{O}[I_{\text{source}}^{\mathbf{x}}(\lambda)R_{\text{FP}}^{\mathbf{x}}(\lambda)R_{\text{lens}}^2(\lambda)R_{\text{FP}}^{\mathbf{z}}(\lambda)T_{\text{FP}}^{\mathbf{y}}(\lambda)]$.

There are $4M^2$ possibilities for secondary lens reflections, from $2M$ lens surfaces. Overall FIIF at pixel $\mathbf{y}$ due to original incidence at pixel $\mathbf{x}$ and intermediate two lens reflections is denoted $F_{\text{FP}}^{\text{single}}(\mathbf{y}, \lambda | \mathbf{x})$. It is of order

$$\mathcal{O}[F_{\text{FP}}^{\text{second}}(\mathbf{y}, \lambda | \mathbf{x})] \sim \tag{8}$$
$$4M^2I_{\text{source}}^{\mathbf{x}}(\lambda)R_{\text{FP}}^{\mathbf{x}}(\lambda)R_{\text{lens}}^2(\lambda)T_{\text{FP}}^{\mathbf{y}}(\lambda)\sum_{\mathbf{z}}R_{\text{FP}}^{\mathbf{z}}(\lambda).$$

The $\mathbf{z}$ summation is over all N_{pixels} pixels on the detector array. For wavelengths that are in $\mathcal{B}(\mathbf{y})$ but not in $\cup\{\mathcal{B}(\mathbf{x}), \mathcal{B}(\mathbf{z})\}$, Eq. (8) degenerates to

$$\mathcal{O}[F_{\text{FP}}^{\text{second}}(\mathbf{y}, \lambda | \mathbf{x})] \sim 4M^2N_{\text{pixels}}I_{\text{source}}^{\mathbf{x}}(\lambda)R_{\text{lens}}^2(\lambda) \tag{9}$$

The magnitude of this component resembles lens-flare, being scaled as $M^2 R_{\text{lens}}^2$.

In careful tests, we found that some reflections are due to the metallic blades of the lens iris. FIIF involving the iris follows similar expressions to Eqs. (6-9), with minor modifications: in Eqs. (6,7), the iris reflectivity R_{iris} is used instead of $2MR_{\text{lens}}$. In Eqs. (8,9), the term $4M^2 R_{\text{lens}}^2$ is replaced either by $4MR_{\text{lens}}R_{\text{iris}}$ (secondary reflections involving a lens and iris) or by R_{iris}^2 (two interactions by the iris).

3.3. Flare Contamination

The scene source is a flare-free spectral image, $I_{\text{source}}^{\mathbf{x}}(\lambda)$, which is generally distributed over a domain of pixels, up to the entire image domain Ω. The total optical power of the source, as measured through the filter array is

$$E_{\text{source}} = \sum_{\mathbf{x} \in \Omega} \int_\lambda I_{\text{source}}^{\mathbf{x}}(\lambda) T_{\text{FP}}^{\mathbf{x}}(\lambda) \mathrm{d}\lambda. \qquad (10)$$

Here wavelength integration is over the sensitivity domain of the detector array beneath the filters, and spatial summation is over all pixels in the image domain.

Overall, FIIF includes many orders of reflections: they involve any number of reflections by optical elements, and all of these orders involve at least one reflection by interference filters. The result of FIIF (of all orders) is a flare image, denoted $F_{\text{FP}}(\mathbf{y}, \lambda)$. The total optical power of FIIF is

$$E_{\text{FP}} = \sum_{\mathbf{y} \in \Omega} \int_\lambda F_{\text{FP}}(\mathbf{y}, \lambda) \mathrm{d}\lambda . \qquad (11)$$

We define the total *FIIF contamination* by

$$C = E_{\text{FP}} / E_{\text{source}} . \qquad (12)$$

4. Simulations of the Phenomenon

To rigorously study FIIF, we used detailed simulations, including optical setups modeled by the Zemax Opticstudio software. Here are their details.

Detector array. An example off-the shelf SHYC is the XIMEA MQ022HG-IM-SM4X4-VIS containing an IMEC SNm4x4-VIS sensor. It is based on interference filters. We matched the simulation to this camera, as much as possible. Correspondingly, the model uses a two-dimensional 1024×2048 array or pixels. Each pixel is covered by a single interference (FP) filter, described below. The pixelated filters are arranged in a 4×4 repetitive pattern (Fig. 6). This setup records hyperspectral images with effective spatial resolution of 256×512 pixels and 16 spectral bands.

FP filters. Each modeled filter is created by modeled mirrors and dielectric glass layers. Filters include metallic
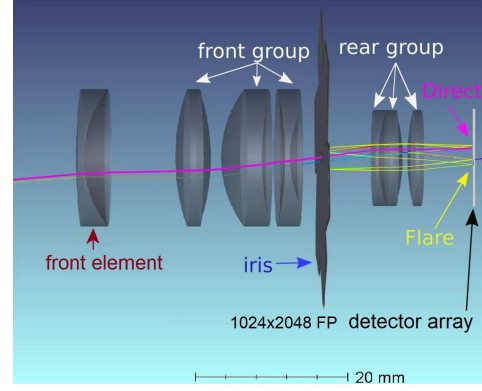

Figure 6. A Layout of a simulated system, including Edmund Optics a #59-870 16mm fixed focal length lens design. This lens consists of 7 lens elements, two triplets and a front collimating lens. This illustration samples a single ray from the source. This ray is reflected by the spectral filter and then splits at lens surfaces.
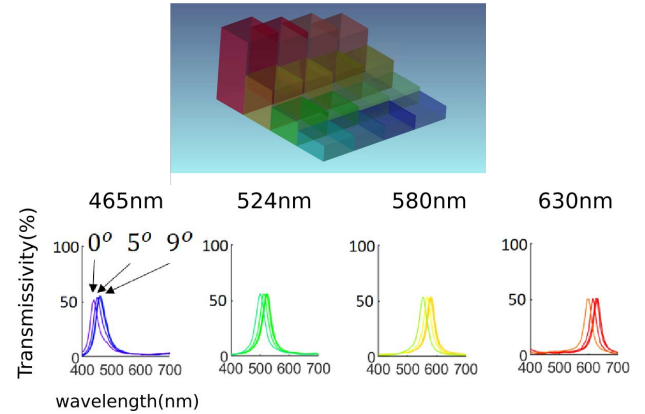

Figure 7. [Top] 3D layout of a single SHYC filter array, arranged into a 4×4 cell. [Bottom] Samples of four out of 16 simulated functions $T_{\text{FP}}^{\mathbf{x}}(\lambda)$. Different filters have a distinguished pass-band, which is somewhat affected by the incidence angle.

surfaces made of silver (Ag) and zinc-sulfide (ZnS), being $0.08 - 0.10\mu\text{m}$ thick, and MGF2 glass layers whose thickness is $1.5 - 2\mu\text{m}$. The Zemax software calculates the spectral transmissivity and reflectivity of each filter, based on these parameters. Consequently, we adjusted the thickness and reflectivity of the layers (Fig. 7), so that the Zemax software yields 16 filters, whose pass-bands resemble those of the SNm4x4-VIS sensor.

Compound Lens. The lens model is a 16mm fixed-focus lens by Edmund Optics, design $\#59 - 870$. It consists of 7 lens elements, as published in [10]. The lens elements in the model have a modelled anti-reflection coating (Fig. 8[Left]).

Iris. The model iris blades are either partly-reflecting metallic (Fig. 8[Right]), or completely absorbing. The iris
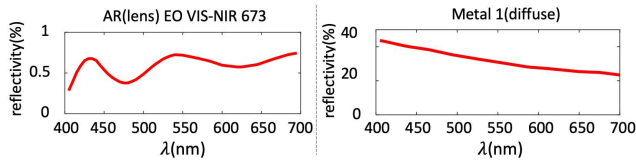
Figure 8. [Left]—Simulated reflectivity of a lens anti-reflection coating [Right] A metallic iris (Zemax-catalogue standard METAL1 coating profile).
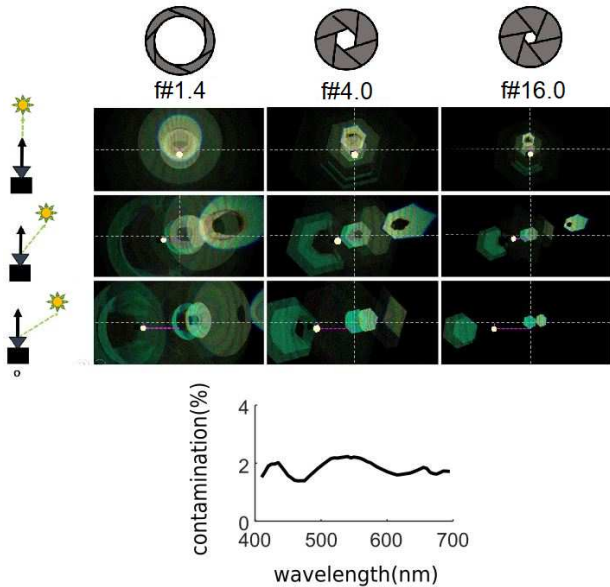

Figure 9. Simulated FIIF. The iris blades are absorptive. [Top] Sample images. [Bottom] FIIF contamination as a function of wavelength, in percents.

is set for $f\# = 1.4, 4, 16$.

Light source. The object is an isotropic point source having a broadband halogen spectrum. It was located either on the optical axis of the camera, or 7.5^o off-axis.

Light transport Each image was rendered by Zemax using 2 million rays. The sampling method of the rays is Sobol Sequences Monte Carlo.

Corresponding to absorbing and metallic iris blades, Figs. 9, 10 depict results using three different aperture sizes and two source locations. Evidently, changing the source position strongly affects the FIIF distribution. Some reflections involve lenses and some involve the iris. Closing the iris reduces FIIF associated with lenses but increases FIIF associated with a metallic-blade iris.

Based on these simulations, we numerically assessed the FIIF contamination C (Eq. 12) as used in SHYCs. In our simulations, we found that C ranges between 2% and 5%. This is much higher than contamination by lens flare in ordinary cameras, which is of $\mathcal{O}(10^{-4})$, as explained in
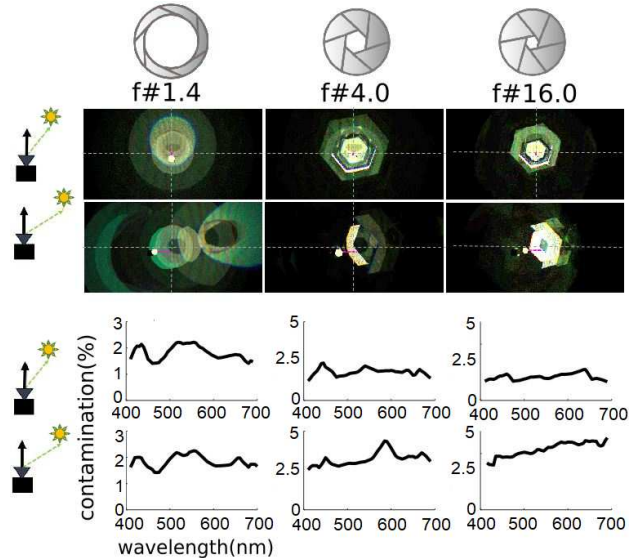

Figure 10. Simulated FIIF. The metallic iris blades are partly reflective. [Top] Sample images. [Bottom] FIIF contamination as a function of wavelength, in percents.

Sec. 2.2.

5. Real-World Experimental Evidence

We demonstrated the magnitude of FIIF using a physical SHYC in real-world experiments. The setup is depicted in Fig. 11. As in the simulations, the experiments use the SHYC model XIMEA MQ022HG-IM-SM4X4-VIS containing an IMEC SNm4x4-VIS sensor. For comparison, the experiments also used a standard camera having an RGB Bayer-mosaic, as a reference. The reference was an IDS-ML camera, which has a TELEDYNE E2V RGB sensor. The two cameras were adjacent, observing the same scenes using a lens of the same model, Edmund Optics 16mm VIS-NIR #67-714[2]. The source was a DC-powered halogen bulb, illuminating through a a diffuser and a pinhole, effectively a small diffuse source.

Images taken by the SHYC are compared in Fig. 12 to images taken by the reference RGB camera. This comparison reveals distinction between lens flare (reported in prior art), to FIIF. The latter is generally brighter and spatially more expansive. Fig. 13 shows images taken with the SHYC, for several off-axis angles and $f\#$ values. FIIF is significant, having wide breadth, and it is much stronger than lens flare. The figure plots the FIIF contamination as a function of wavelength. In all experiments, $C \sim 5\%$.

In addition to intensity changes, FIIF has a qualitative effect as it alters the acquired spectra in the affected sensor areas, demonstrated in Fig. 14[top]. To quantify the effect we

---

[2]We could not find a public Zemax model for this lens. Therefore, the simulations used a slightly different lens.
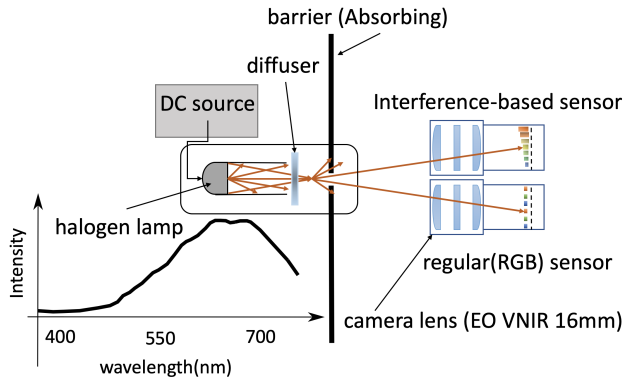
Figure 11. Depiction of our experimental setup. We placed an RGB camera next to a SHYC. Both imaged the same light source using lenses of the same model and settings. We used a 40W halogen bulb placed behind the barrier.
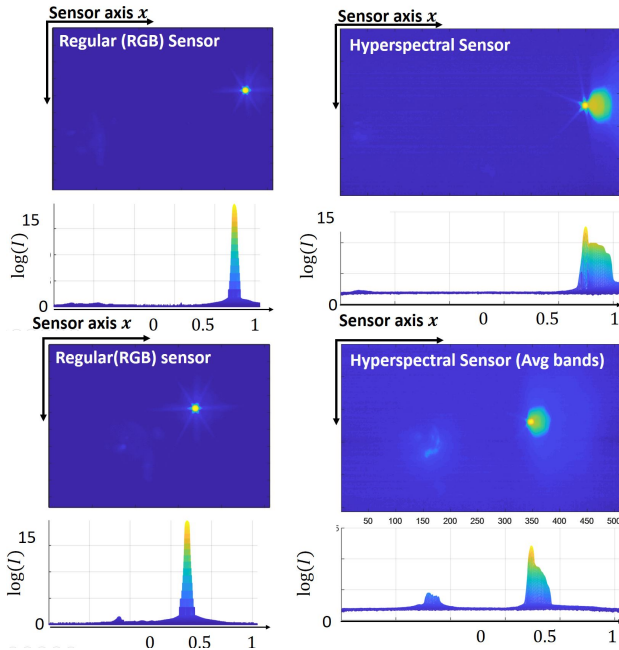

Figure 12. [Left] High dynamic range measurements from our experimental setup, using an RGB camera. [Right] High dynamic range measurements of the same setup, using a SHYC. FIIF has a wider spatial spread than lens-flare.

imaged a color chart with our SHYC. The measured spectra differ from the published ground truth ones. For validation, Fig. 14[bottom] depicts the SHYC spectral readings of the same color chart under lighting conditions that resulted in less FIIF. There the measurements are very close to the ground truth spectra. Following standard conduct, the reflectance was calculated by dividing the measurements by the gray patch measurement, which by itself may contain FIIF. Nevertheless, the spectral effect of the FIIF is still visible.
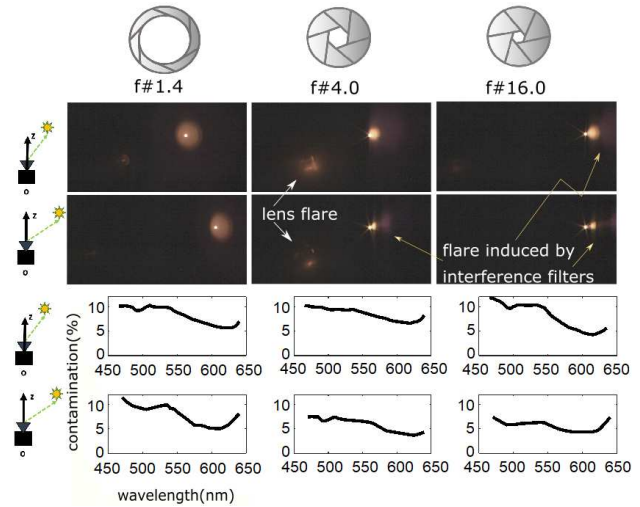

Figure 13. [Top] Images of a small source (halogen lamp) and the resulting FIIF at different spatial positions and $f\#$ values. [Bottom] The contamination C in each of these setups.

6. Deflaring of Wide-Field Scenes

We demonstrate partial digital reduction of FIIF in experiments. The experimental scenes were dense and wide-field, i.e., not point sources. Consequently, many areas stretching the extent of the FOV create FIIF. Hence, the FIIF is very smooth and broad, spanning major regions of the FOV. This is contrary to typical lens-flare, which is typically created by the sun or other sparse and extremely bright point sources.

The method of Ref. [22] relies on a long sequence of the scene, acquired through a large mask that includes occluding barriers. Its drawback is long acquisition time, which implies imaging of static scenes. However, it is suitable for diffuse flare, and indeed it was effective in our experiment, summarized in Fig. 15.

Deflaring by motion [12] uses a very short sequence of raw images taken while the camera slightly rotates laterally. It is fast. However, post-processing in [12] exploits the fact that lens-flare is typically spatially limited to a vicinity of a line between two points: the projection of the sun (or another bright point source) and the projection of the optical axis. This is *not* the nature of FIIF caused by broad areas having ordinary scene points. Hence, the approach of [12] had only moderate success in countering FIIF. This experiment is summarized in Fig. 16.

7. Discussion

The paper points out a significant and unreported drawback of SHYCs that are based on interference filters. Narrow-band transmissive interference filters are highly reflective by nature. Embedded inside a camera, they create strong stray light, which leads to strong and spatially broad FIIF. The FIIF biases hyperspectral measurements of any
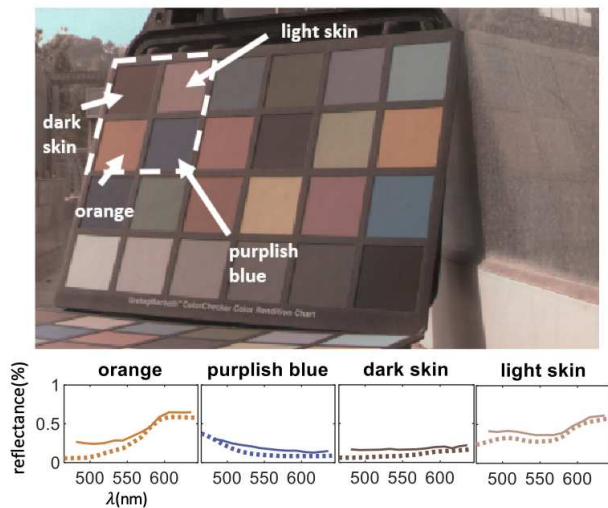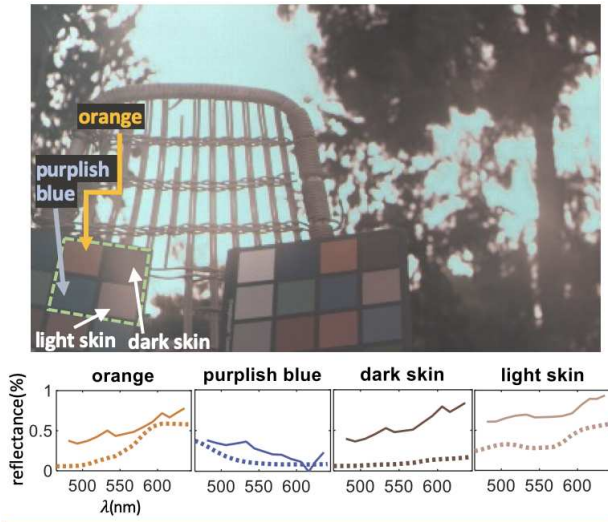
Figure 14. FIIF has a qualitative effect as it changes the shape of the measured spectra. [Top] Image of a color chart back lit by a diffuse sky, recorded using our SHYC. The FIIF is broad. It affects the measured spectra of the color patches (solid lines), which differ from the ground truth spectra (dotted lines). [Bottom] The same color chart is imaged under different lighting conditions that result in less FIIF. Then, the measured spectra (solid) are very similar to the ground truth spectra (dotted).

point, and this bias depends on the scene, i.e. on spectral content in independent scene points.

We tested prior deflaring methods to counter FIIF. However, not all prior methods can suit FIIF. The interesting nature of FIIF calls for newer deflaring methods. In addition, it is possible that stronger solutions would involve optical hardware methods to counter stray light. For example, the Scheimpflug principle enables the sensor plane to be tilted relative to the optical axis of the lens, while keeping the object focused. In a tilted sensor-plane, stray light reflected by the attached FP filters may significantly miss-out the lens
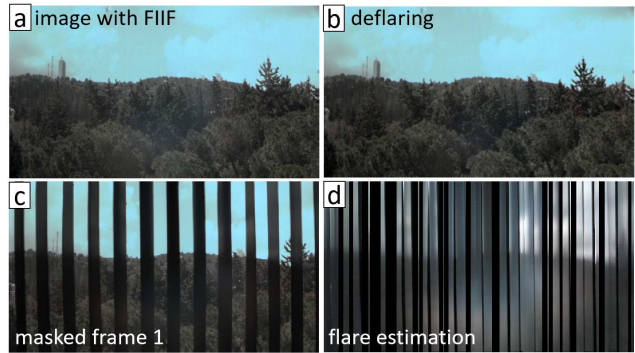

Figure 15. a) The entire scene with FIIF. b) The deflared scene. c) One of the four frames we acquired of the scene, imaged through a barrier that was shifted quickly across the scene. d) The estimated flare. The flare has partial vertical patterns due to the barrier's shape.
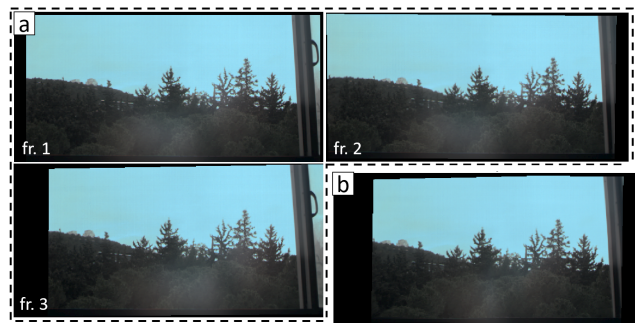

Figure 16. a) Three out of four acquired images of an outdoor scenes. The camera slightly rotated laterally between frames. FIIF is strong. b) Result of deflaring using [12]. The improvement is only moderate, because FIIF is very broad by nature.

elements, thereby reducing FIIF optically.

More interesting may be holistic approaches to optical design, image sequences and post-processing algorithms, to counter FIIF. For example, each spectral filter may multiplex several wavelength bands, so as to reduce reflection, and spectral demultiplexing can be done computationally in post-processing [2, 16]. Interference filters may include lossy materials to reduce reflections, and lens anti-reflection coatings may need to be co-designed with the hyperspectral filters.

Acknowledgements

References

[1] Helge Aasen, Andreas Burkart, Andreas Bolten, and Georg Bareth. Generating 3D hyperspectral information with lightweight UAV snapshot cameras for vegetation monitoring: From camera calibration to quality assurance. *ISPRS J. of Photogrammetry and Remote Sensing*, 108:245–259, 2015. 1

[2] Marina Alterman, Yoav Y. Schechner, and Aryeh Weiss. Multiplexed fluorescence unmixing. In *Proc. IEEE ICCP*. IEEE, 2010. 8

[3] Boaz Arad and Ohad Ben-Shahar. Filter selection for hyperspectral estimation. In *Proc. IEEE ICCV*, pages 3153–3161, 2017. 1

[4] Floris Chabert. Automated lens flare removal. Technical report, Stanford University, Department of Electrical Engineering, 2015. 2

[5] Ayan Chakrabarti and Todd Zickler. Statistics of real-world hyperspectral images. In *Proc. IEEE CVPR*, pages 193–200, 2011. 1

[6] Ying Fu, Tao Zhang, Yinqiang Zheng, Debing Zhang, and Hua Huang. Joint camera spectral sensitivity selection and hyperspectral image recovery. In *Proc. ECCV*, pages 788–804, 2018. 1

[7] Gonzalo Hernández. *Fabry-Perot Interferometers*. Cambridge University Press, 1988. 1

[8] Matthias Hullin, Elmar Eisemann, Hans-Peter Seidel, and Sungkil Lee. Physically-based real-time lens flare rendering. *ACM Trans. Graphics (TOG)*, 30(4):108, 2011. 2

[9] Nur Ismail, Cristine Calil Kores, Dimitri Geskus, and Markus Pollnau. Fabry-pérot resonator: spectral line shapes, generic and related airy distributions, linewidths, finesses, and performance at low or frequency-dependent reflectivity. *Optics express*, 24(15):16366–16389, 2016. 2

[10] Rhiannon Katarina Jenkins. The effect of adding an aspherical surfaces to a fixed-focal-length lens. M.Sc. thesis, University of Arizona, 2016. 5

[11] Joel Kaluzny, Hao Li, Wenzhong Liu, Peter Nesper, Justin Park, Hao F Zhang, and Amani A Fawzi. Bayer filter snapshot hyperspectral fundus camera for human retinal imaging. *Current Eye Research*, 42(4):629–635, 2017. 1

[12] Fima Koreban and Yoav Y. Schechner. Geometry by deflaring. In *Proc. IEEE ICCP*, 2009. 2, 4, 7, 8

[13] Norman Koren. Measuring the impact of flare light on dynamic range. *Electronic Imaging*, 2018(12):169–1, 2018. 3

[14] Charis Lanaras, Emmanuel Baltsavias, and Konrad Schindler. Hyperspectral super-resolution by coupled spectral unmixing. In *Proc. IEEE ICCV*, pages 3586–3594, 2015. 1

[15] Aviad Levis, Yoav Y. Schechner, and Anthony B. Davis. Multiple-scattering microphysics tomography. In *Proc. IEEE CVPR*, pages 6740–6749, 2017. 1

[16] Moran Mordechay and Yoav Y. Schechner. Matrix optimization for poisson compressed sensing. In *IEEE Global Conf. on Signal and Information Processing*, pages 684–688, 2014. 8

[17] Julien Pichette, Audrey Laurence, Leticia Angulo, Frederic Lesage, Alain Bouthillier, Dang Khoa Nguyen, and Frederic Leblond. Intraoperative video-rate hemodynamic response assessment in human cortex using snapshot hyperspectral optical imaging. *Neurophotonics*, 3(4):045003, 2016. 1

[18] Ramesh Raskar, Amit Agrawal, Cyrus A. Wilson, and Ashok Veeraraghavan. Glare aware photography: 4D ray sampling for reducing glare effects of camera lenses. *ACM Trans. Graphics (TOG)*, 27(3):56, 2008. 2

[19] Dikpal Reddy and Ashok Veeraraghavan. Lens flare and lens glare. *Computer Vision: A Reference Guide, Springer*, pages 445–447, 2014. 3

[20] Yoav Y. Schechner and Shree K. Nayar. Uncontrolled modulation imaging. In *Proc. IEEE CVPR*, 2004. 1

[21] Mary Caswell Stoddard, Audrey E. Miller, Harold N. Eyster, and Derya Akkaynak. I see your false colours: how artificial stimuli appear to different animal viewers. *J. of the Royal Society Interface Focus*, 9(1):20180053, 2018. 1

[22] Eino-Ville Talvala, Andrew Adams, Mark Horowitz, and Marc Levoy. Veiling glare in high dynamic range imaging. In *ACM Trans. Graphics (TOG)*, volume 26, page 37, 2007. 2, 4, 7

[23] Labrinus Van Manen, Jeroen Eggermont, Oleh Dzyubachyk, Arantza Fariña-Sarasqueta, Alexander Vahrmeijer, Sven Mieog, and Jouke Dijkstra. Snapshot hyperspectral imaging for detection of breast tumors in resected specimens. In *Diseases in the Breast and Reproductive System V*, volume 10856, page 108560I. Int. Society for Optics and Photonics, 2019. 1

[24] Tai-Pang Wu and Chi-Keung Tang. A bayesian approach for shadow extraction from a single image. In *Proc. IEEE ICCV*, pages 480–487, 2005. 2

[25] Seoung Wug Oh, Michael S. Brown, Marc Pollefeys, and Seon Joo Kim. Do it yourself hyperspectral imaging with everyday digital cameras. In *Proc. IEEE CVPR*, pages 2461–2469, 2016. 1

[26] Ximea. Xispec hyperspectral cameras brochure. https://www.ximea.com/files/brochures/xiSpec-Hyperspectral-cameras-2015-brochure.pdf. 1

[27] Zhiwei Xiong, Lizhi Wang, Huiqun Li, Dong Liu, and Feng Wu. Snapshot hyperspectral light field imaging. In *Proc. IEEE CVPR*, pages 3270–3278, 2017. 1

[28] Yanfei Zhong, Xinyu Wang, Yao Xu, Shaoyu Wang, Tianyi Jia, Xin Hu, Ji Zhao, Lifei Wei, and Liangpei Zhang. Mini-UAV-borne hyperspectral remote sensing: From observation and processing to applications. *IEEE Geoscience and Remote Sensing Magazine*, 6(4):46–62, 2018. 1

[29] Kang Zhu, Yujia Xue, Qiang Fu, Sing Bing Kang, Xilin Chen, and Jingyi Yu. Hyperspectral light field stereo matching. *IEEE Trans. PAMI*, 2018. 1

[30] Adi Zweifler, Derya Akkaynak, Tali Mass, and Tali Treibitz. *In situ* analysis of coral recruits using fluorescence imaging. *Frontiers in Marine Science*, 4:273, 2017. 1